ACCSCIENCE PUBLISHING

Materials Science in Additive Manufacturing

ORIGINAL RESEARCH ARTICLE

Computed tomography and finite element analysis-optimized Ti6Al4V bone plate combined with a porous 3D β-tricalcium phosphate cage for repairing segmental tibial defects in rabbits

Supplementary File

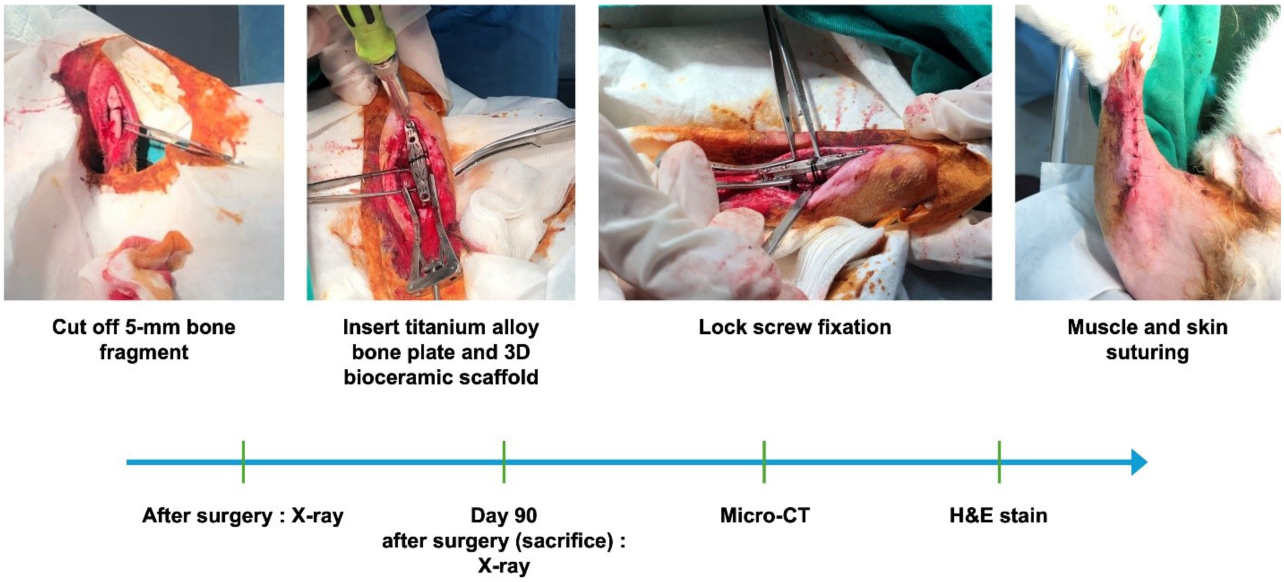

Figure S1. Schematic illustration of the surgical procedure and evaluation timeline for rabbit tibial segmental defect repair. The study consisted of three main stages. First, a 5-mm segmental defect was created in the mid-diaphysis of the rabbit tibia to establish a standardized bone defect model for evaluating implant fixation and early bone regeneration. Second, the defect was stabilized using an FEA-optimized 3D-printed Ti6Al4V bone plate, and the defect gap was paired with a 3D-printed interconnected porous bioceramic cage designed to match the defect geometry. The porous cage served as an osteoconductive scaffold to support tissue infiltration and new bone formation. Third, at 90 days after surgery, the animals were sacrificed for ex vivo evaluation, including micro-CT and histological analysis. These assessments were used to examine implant stability, bone ingrowth, scaffold–tissue integration, and defect repair within the regenerated region.
Abbreviations: CT: Computed tomography; FEA: Finite element analysis; H&E: Hematoxylin and eosin.

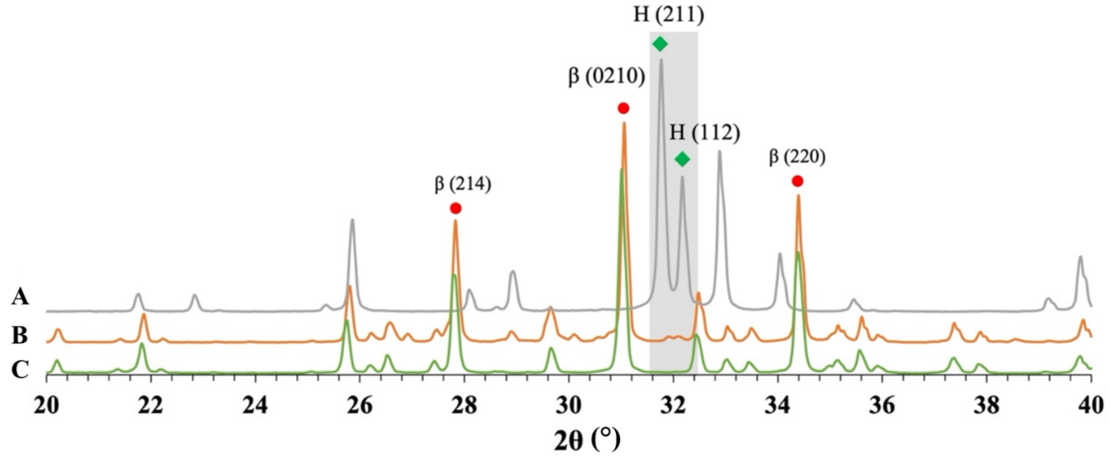

Figure S2. X-ray diffraction (XRD) patterns of the starting powders and the sintered 3D-printed interconnected porous bioceramic scaffold. The diffraction patterns correspond to (A) hydroxyapatite (HAp) powder, (B) β-tricalcium phosphate (β-TCP) powder, and (C) the 3D bioceramic scaffold after sintering at 1,150°C. Characteristic HAp peaks are marked with ◆ (JCPDS PDF No. 09-0432), and β-TCP peaks are marked with ● (JCPDS PDF No. 09-0169). The XRD pattern of the sintered scaffold indicates that β-TCP was the predominant crystalline phase after sintering. The conversion of HAp to β-TCP occurs at elevated temperatures, typically above 1,100°C. HAp is a stable compound under physiological conditions, but it becomes thermodynamically unstable at high temperatures due to the loss of its hydroxyl groups (OH^-). This dehydration process is irreversible and leads to the formation of a different crystalline phase. The primary mechanism is the dehydroxylation of HAp, in which hydroxyl ions leave the crystal lattice, often reacting with one another to form water vapor. This reaction can be simplified as:

$$Ca_{10}(PO_4)_6(OH)_2 \xrightarrow{Heat} 3Ca_3(PO_4)_2 + CaO + H_2O\uparrow$$

The calcium oxide (CaO) byproduct is often incorporated into the β-TCP lattice or reacts further, leading to a complex phase diagram. The final composition of the material after sintering is highly dependent on the initial stoichiometry, temperature, and atmospheric conditions.[1,2] In our study, the bottom XRD pattern is for pure raw HAp powder, with peaks labeled H(211) and H(112) at around 31.8° and 32.2°, respectively. The middle XRD pattern is for pure raw β-TCP powder. The peak labeled β(0210) at approximately 31° is a characteristic peak for β-TCP. The after-sintered 3D-printed interconnected porous bioceramic indicates its 100% β-TCP crystalline structure. For example, this peak confirms that the material is indeed β-TCP without any detectable HAp or other phases. The combination of β-TCP and HAp in the raw materials (70% β-TCP + 30% HAp) will accelerate β-TCP degradation, allowing space for new bone growth.

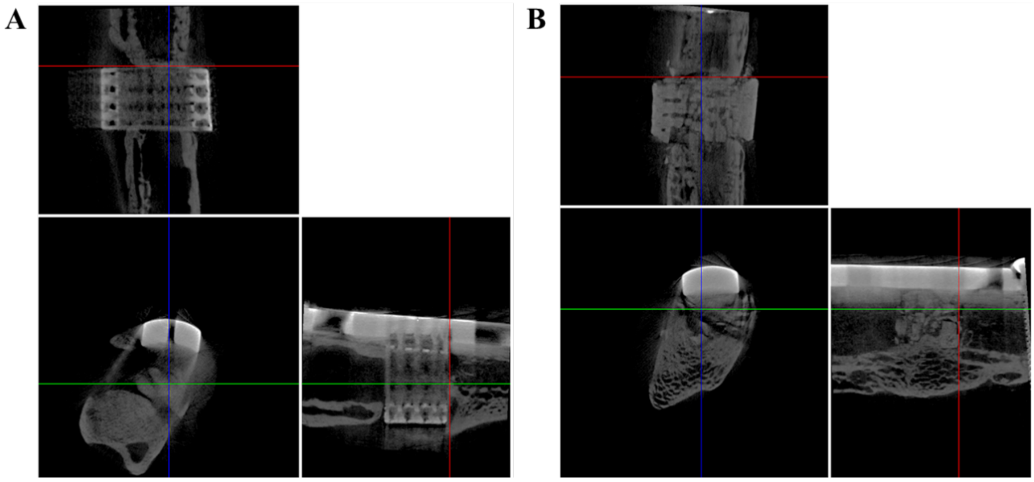

Figure S3. In situ micro-computed tomography (CT) images of rabbit tibial segmental defects after implantation of two fixation constructs: (A) the finite element analysis (FEA)-optimized 3D-printed Ti6Al4V bone plate (3D Ti6Al4V-BP) integrated with a gradient-porous Ti6Al4V cage, and (B) the FEA-optimized 3D Ti6Al4V-BP paired with an interconnected porous 3D bioceramic cage. Representative sagittal (upper left), axial (lower left), and coronal (lower right) views are shown. The in situ micro-CT scans obtained at 35 μm resolution for both fixation systems were severely affected by metal-induced artifacts originating from the Ti6Al4V bone plate. In (A), image degradation was further exacerbated because the gradient-porous cage was also composed of Ti6Al4V, resulting in substantial interference from both metallic components. Consequently, the scaffold, newly formed bone, and surrounding host tissue could not be reliably distinguished. In (B), although the interconnected porous bioceramic cage was expected to generate less radiographic interference than the metallic cage, artifacts from the Ti6Al4V bone plate still dominated the images, obscuring detailed visualization of the scaffold architecture and tissue ingrowth.

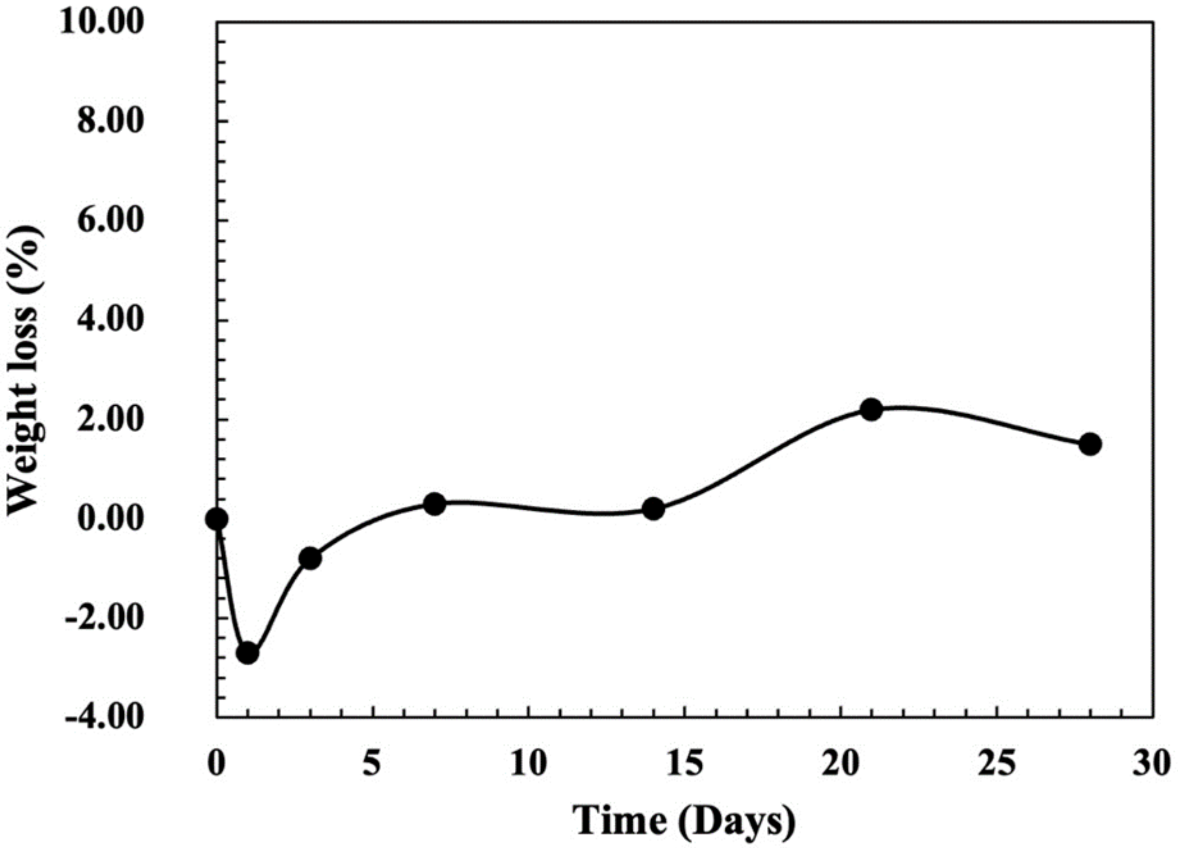

Figure S4. The percent weight loss by interconnected porous 3D bioceramic immersed in phosphate-buffered saline (PBS) as a function of time (*n* = 3). The degradation behavior of the β-tricalcium phosphate (β-TCP) cage was evaluated by immersing specimens in PBS at 37 ± 1 °C for 28 days. At each designated time point, specimens were removed, rinsed with distilled water, and dried in a vacuum oven for 24 h prior to weighing. Mass loss was calculated as the mean of three independent samples according to the following equation:

$$\text{Weight loss}(\%) = 100 \times \frac{(\text{Wo} - \text{Wt})}{\text{Wo}} \quad \textbf{(S1)}$$

where W_o is the starting dry weight, and W_t is the dry weight at time t. Over the 28-day immersion period, the β-TCP cage demonstrated a cumulative mass loss of approximately 1.5%, indicating a relatively slow degradation profile under simulated physiological conditions.

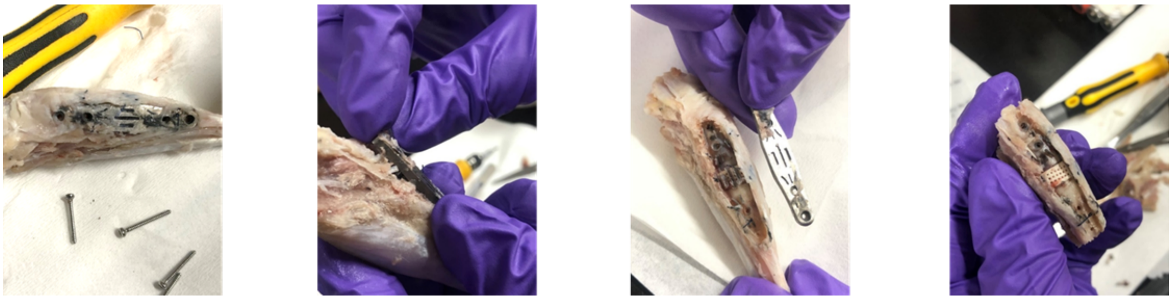

Figure S5. Schematic diagram illustrating the removal of a Ti6Al4V bone plate from the left tibia of a rabbit in an animal experiment, 90 days post-surgery. These metal-induced artifacts, including streaking and shadowing, prevented reliable assessment of scaffold microstructure, such as the gradient porosity in the finite element analysis (FEA)-optimized 3D-printed Ti6Al4V bone plate (3D Ti6Al4V-BP) integrated with a gradient-porous Ti6Al4V cage and the interconnected pore channels in the FEA-optimized 3D Ti6Al4V-BP paired with an interconnected porous 3D bioceramic cage, and also precluded accurate quantitative analysis of bone regeneration within the defect region. Accordingly, parameters such as new bone volume, trabecular morphometric indices, and scaffold degradation could not be reliably measured from these in situ scans. To overcome these limitations, complementary approaches such as histological analysis and ex vivo micro-computed tomography after removal of the Ti6Al4V bone plate were necessary for subsequent evaluation.

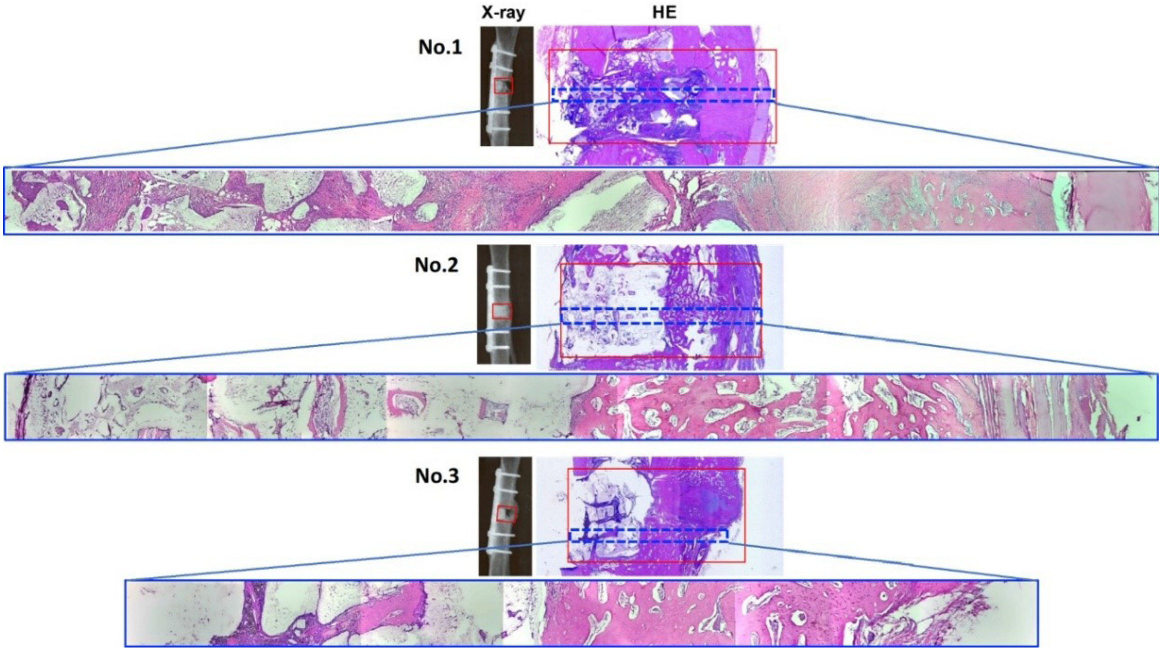

Figure S6. Representative radiographic and hematoxylin and eosin (H&E)-stained histological images of whole tibial defect specimens from three rabbits (n = 3), 90 days after implantation of the finite element analysis (FEA)-optimized 3D-printed Ti6Al4V bone plate (3D Ti6Al4V-BP) paired with an interconnected porous 3D bioceramic cage in a rabbit tibial segmental defect model. Corresponding X-ray and histological images are shown for each specimen. Specimens No. 2 and No. 3 showed more extensive decalcified void-like regions corresponding to the former bioceramic scaffold than specimen No. 1, indicating that substantial scaffold remnants were still present before decalcification at 90 days. This observation is consistent with the relatively slow resorption behavior observed in the densified β-TCP-based bioceramics in this study.[3] The persistence of the scaffold at this stage may be beneficial, as it helps maintain structural support while allowing progressive tissue ingrowth and defect repair. In this hybrid construct, the interconnected porous 3D bioceramic cage potentially facilitated cell infiltration and nutrient transport, whereas the Ti6Al4V bone plate provided rigid external fixation of the tibial defect. Notably, some specimens appeared to show more advanced new bone formation in regions farther from the bone plate than in regions immediately adjacent to it. Although this pattern cannot be conclusively determined from histology alone, it may reflect local differences in mechanical stimulation and vascular access. Areas closer to the rigid plate may have experienced reduced physiological loading, whereas regions farther from the plate may have provided a more favorable environment for bone formation.[4-6] In addition, prominent early callus tissue was not a dominant feature at 90 days, suggesting that healing in some regions had progressed beyond the early reparative stage toward more organized bone matrix formation. However, inter-animal variability remained evident, with specimens No. 2 and No. 3 still showing less mature repair tissue than specimen No. 1. Overall, these findings support the interpretation that the interconnected porous 3D bioceramic cage provided a stable osteoconductive framework for progressive bone regeneration within the segmental defect.[7]

References

1. Suchanek W, Yoshimura M. Processing and properties of hydroxyapatite-based biomaterials for use as hard tissue replacement implants. *J Mater Res*. 1998;13(1):94-117.

   doi: 10.1557/JMR.1998.0015

2. Moslim NA, Beh CY, Kasim SR, Ramakrishnan S. Effect of composition and temperature to the HA/β-TCP composite. *J Phys: Conf Ser*. 2018;1082(1):012023.

   doi: 10.1088/1742-6596/1082/1/012023

3. Al-allaq AA, Kashan JS. A review: In vivo studies of bioceramics as bone substitute materials. *Nano Select*. 2023;4:123-144.

   doi: 10.1002/nano.202200222

4. Robling AG, Turner CH. Mechanical signaling for bone modeling and remodeling. *Crit Rev Eukaryot Gene Expr*. 2009;19(4):319-338.

   doi: 10.1615/critreveukargeneexpr.v19.i4.50

5. Rücker M, Laschke MW, Junker D, *et al*. Vascularization and biocompatibility of scaffolds consisting of different calcium phosphate compounds. *J Biomed Mater Res A*. 2008;86(4):1002-1011.

   doi: 10.1002/jbm.a.31722

6. Field JR, Sumner-Smith G. Bone blood flow response to surgical trauma. *Injury*. 2002;33(5):447-451.

   doi: 10.1016/s0020-1383(02)00014-1

7. Zhang B, Xing F, Chen L, *et al*. DLP fabrication of customized porous bioceramics with osteoinduction ability for remote isolation bone regeneration. *Biomater Adv*. 2023;145:213261.

   doi: 10.1016/j.bioadv.2022.213261